Experimental and Numerical Investigation of Pulverized Biomass Flames in a Pilot-scale Reactor Using OH* Chemiluminescence Imaging and In-flame Probing Techniques

David Honoré, Hassan Mohanna, Carole Gobin, Benoît Taupin, Partick Levy, Jean-Michel Commandré, Bruno Piriou

Experimental and Numerical Investigation of Pulverized Biomass Flames in a Pilot-scale Reactor Using OH* Chemiluminescence Imaging and In-flame Probing Techniques

Hassan Mohanna[a,b,c], David Honoré[b], Carole Gobin[b], Benoit Taupin[a], Patrick Levy[a], Jean-Michel Commandré[c], Bruno Piriou[c]

[a] Veolia Recherche et Innovation (VeRI), 78520 Limay, France
[b] Normandie Univ, INSA Rouen, UNIROUEN, CNRS, CORIA, 76000 Rouen, France
[c] CIRAD UPR BioWooEB, 34398 Montpellier, France

ABSTRACT: An experimental study is performed on a pilot-scale combustion facility to evaluate the structure and characteristics of pulverized biomass flames. The design of the 20kW burner and the combustion chamber is made in a way to allow analyzing the different involved phenomena using OH* chemiluminescence imaging and in-flame measurements of gas concentrations. The characterization of the flames of pine, moderately torrefied pine and pyrolyzed pine, was completed by a CFD simulation, which predicted the aerodynamics, trajectory of the particles, and their degradation process. The chemiluminescence signal of OH* marks the reaction zone of volatiles. The intensity of the signal is strongly dependent on the volatile content. However, the position and size of the reaction zone is rather affected by the particle size distribution than by the biomass thermal treatment. The wide particle size distribution of pine produces a two-stage devolatilization, promoting the reduction of NOx fraction in the second devolatilization region. Higher and earlier devolatilization, oxygen consumption and temperature rise are detected for the treated pine compared to their raw counterpart. The added heat in the recirculation zone helps heating the injected air and biomass which increases flame stability of the finer torrefied and pyrolyzed fuels.
KEYWORDS: Biomass, Combustion, OH* chemiluminescence, Modeling.

1 Introduction

In the view of the increasing demand of energy, the abundance and sustainability of biomass sources present biomass as an important fuel for energy production. This beside the threat of the environmental impact of fossil fuels and the increasing anxiety about their availability at economically acceptable cost, drive the global interest in biomass as a potential fuel for the energy transition. Official European reports estimate that the primary potential of biomass in Europe will represent 15-16% of the projected energy consumption of the EU by 2030 [1]. This significant amount of available biomass can support ambitious renewable energy targets under the current environmental constraints.

At present, one of the main challenges is to develop efficient recovery sectors for biomass. Direct combustion in a furnace is the most common method of producing heat from biomass to generate hot water or steam. The pulverized combustion mode is actually considered as the most efficient, the excess air can be kept very low. Recently, the pulverized combustion of biomass and the co-firing of biomass with coal has raised interest to reduce the CO2 footprint of coal fired power plants. Several coal power plants have been subject to co-firing projects. In Lodz in Poland, three cogeneration units have been installed on existing coal-fired power plants, making the co-combustion of coal and biomass from regional forestry operations possible [2]. In addition, some coal power plants even totally converted their consumption to biomass-derived fuels [3], [4]. However, the pulverized combustion process is largely dependent on the flame structure, which in turn is mainly driven by the biomass characteristics. This can significantly change the operation of the boiler. As a result, a better understanding of the combustion of pulverized biomass is important in the dual objective of improving the energy efficiency and reducing the environmental impact.

The combustion of biomass has been extensively studied at particle scale. However, studies at flame scale are less common in literature as they require the expensive construction and operation of pilot scale facilities. Such experiments are nevertheless necessary and practical to represent the operating conditions encountered at full industrial scale. They give access to the assessment of flow conditions and to detailed measurements of the flame, in a similar manner to controlled laboratory-scale flames. Elfasakhany et al. [5] carried out experimental and numerical investigations of pulverized wood flames in a laboratory vertical furnace. The results described the flame structure and methods to control the flame for lower emissions. Weber et al. [6] also studied the combustion of biomass in jet flames and analyzed the gas distribution and the deposition propensity of biomass particles. Ballester et al. [7] investigated experimentally the biomass flames in more turbulent conditions in a semi-industrial scale reactor. The wide size distribution of biomass particles promotes the existence of two reaction zones along the axis of the furnace, where small particles burn in the first stage while the secondary stage is where the larger particles complete devolatilization and burn.

The research on the combustion of pulverized biomass as a standalone fuel is rather new and a few techniques have been applied, especially advanced non-intrusive techniques. The limited knowledge of the aerodynamic effect on biomass flames set limitations for development of new burner geometries. For this reason, we developed a 20kW down-fired pilot scale reactor dedicated to gain additional deeper understanding of the flame structures of pulverized biomass. The reactor is designed to give access for non-intrusive flame diagnostic techniques like chemiluminescence imaging and particle image velocimetry. This paper reports a series of experiments on the reactor providing in-flame measurements of gas distribution and employing chemiluminescence imaging to study the volatile reaction zone. The data provide information about the flame structure and emissions, and about the particle history inside the flame. Different fuels types are tested so that the influence of fuel variation on the flame structure is assessed. Moreover, a numerical study is carried out to assist the analysis of the experimental data and gain further information of the particle trajectories and the

aerodynamic features of the flow. These features are to be validated in future studies on the reactor using non-intrusive flow field measurements.

2 EXPERIMENTAL METHODS

2.1 The pulverized biomass pilot facility

The experiments were conducted on a 20kW pilot scale reactor designed for the study of pulverized fuel flames. The reactor presented in figure 1 is cylindrical and held vertically to avoid the formation of asymmetric bended flames that would appear due to the buoyancy effect. The combustion chamber is composed of five segments standing to 3700 mm length with an inner diameter of 400 mm. The 200 mm thick wall is made of several layers of refractory concrete and insulating materials that can withstand the combustion environment and limit the heat loss. Seventeen circular ports (ø80 mm) and seventeen rectangular ports (80 x 20 mm) are fitted along the furnace with close meshing near the burner and more distant locations downwards. These ports give access to probes for in-flame measurements and non-intrusive optical diagnostics of the flame. When not used for measurements, the ports are closed with plugs made of insulating concrete in order to limit the heat loss through them. The plugs can serve also as stands for K-type thermocouples to measure the wall temperature distribution.

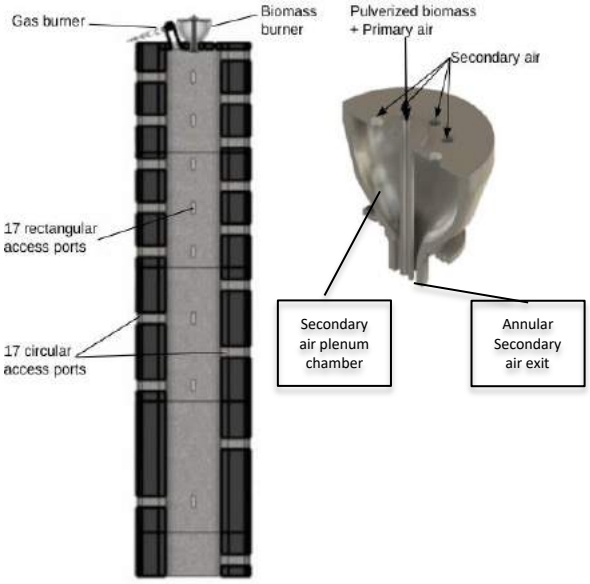

Figure 1: Schematic representation of the pilot scale reactor and the biomass burner

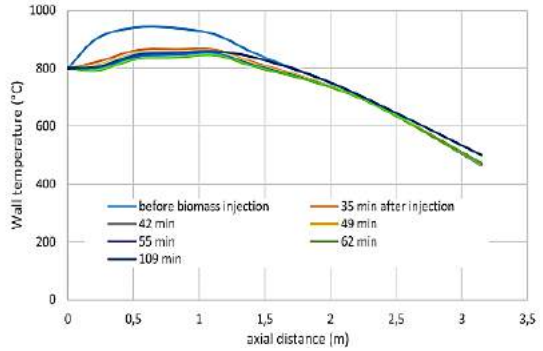

Figure 2: Wall temperature before biomass injection and during an hour of Pin-T flame reaching steady state

The biomass burner mounted on top of the reactor is a bluff-body burner capable of generating a long stable flame suitable for the study of turbulence-chemistry interactions and it bears a great similarity to practical combustors used in many industrial applications. The burner consists of two concentric tubes in which fuel is delivered pneumatically to the central annular tube, while the combustion air is heated to 380°C and injected through the outer tube. Due to the high airflow rate in the annular section, the secondary injection was designed with a plenum chamber and a convergent nozzle to reduce the mean-flow non-uniformities and to produce a controlled velocity profile at the burner outlet.

Prior to an experiment, the chamber is heated for an entire night using a 50 kW natural gas burner mounted next to the biomass burner. The burner power is controlled so that the temperature of the chamber does not surpass 1000°C. Once the upper section of the chamber reaches the defined temperature (950°C), pulverized biomass is injected and the gas burner is shut-off. The flame is left for 20 to 30 minutes to reach the steady state temperature (see figure 2). At steady state, the first and second sections reach approximately 847°C and the temperature of the lower sections increases slightly. The temperature profile is preserved during the experiment that may last up to two hours.

2.2 OH* chemiluminescence imaging

The use of a specific sensor, sensitive in ultraviolet, visible or infrared range is relevant for analyzing the quality of combustion. The chemiluminescence being locally generated in an exothermic combustion zone, its recording with a two-dimensional sensor produces instantaneous images of the reaction zones. This diagnosis is relatively simple to implement, but it requires sensitive equipment because of the low signal level. For flames with a strong soot radiation (yellow flame oil, wood or coal) or in a hot radiating environment as a furnace, the use of a UV detector is preferred to better filter the reaction zone emission from other radiations by collecting OH* chemiluminescence centred at 308 nm.

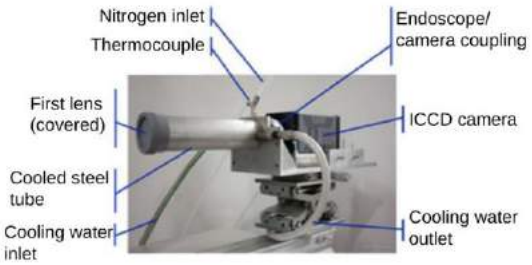

Figure 3: The water-cooled flamoscope used for the measurement of OH* chemiluminescence signal

For the imaging of the OH* chemiluminescence signal, a new collection system (flamoscope) consisting of a water-cooled UV-VIS endoscope has been implemented on the biomass reactor. The flamoscope presented in figure 3 consists of an optical system divided into five groups of lenses made of materials adapted to the visible and ultraviolet spectral range. The lenses construct and transport the image to the photocathode of the intensified camera emICCD Princeton Instruments PIMAX4 (1024 x 1024 pixels - 16 bits) which large and high dynamic range sensor provides high sensitivity and optimized spatial resolution for chemiluminescence

imaging of large flames. This optical assembly with a total length of 370 mm is equivalent to a reflex photographic lens of the 'fisheye' type with a focal length of 12.8 mm for an aperture of f/3.9, with an extended focus range (0.2 m - ∞), a large field depth, low geometric distortion and a wide field of vision. The set of lenses is placed in a stainless-steel sheath cooled by water circulation. A flow of dry air passes through the optical tube and exits from a small pupil to thermally and mechanically protect the first lens. The coupling between the endoscope and the emICCD camera is carried out with a differential thread ring for fine adjustment of the focus. This same ring accommodates the spectral filters chosen for the spectral selection of the chemiluminescence in UV.

When inserted 14 cm inside the furnace wall, the flamoscope allows to acquire four times the field of view obtained by a camera outside the chamber in a standard configuration. This large field of view (270 x 270 mm²) and the chosen distance between two successive optical accesses allow us to have a quasi-continuity of the image of the reaction zone in the combustion chamber. The camera is mounted on a 3-axe moving precise robot fixed on a 4 m lifting table. The camera is calibrated with a reference grid of UV LEDs outside and inside the chamber to determine magnification ratio.

The recorded chemiluminescence images are digitized with a 16 bits dynamic range of 65,535 gray levels. The exposure times are around 400 to 750 µs in order to take full advantage of the sensor capacity under different signal intensities, resulting from the different positions in the flame and different operating conditions. The intensifier gain is set close to the maximum value (9000). Each access point is the subject of a series of acquisitions with at least 2000 images at an acquisition frequency of 5 Hz. These images are used to calculate an average flame image.

2.3 In-flame species measurements by gas sampling

A sampling probe is used to carry out the gas sampling in order to measure the species distribution inside the flame. The probe is a 1.6 m tube of 5 mm internal diameter, protected by another 8 mm diameter tube. Due to operating difficulties such as tar and water condensation blocking the probe, the sampling was conducted without water cooling. Considering the relatively small diameter of the chamber and the thick insulation layer, the temperature of the extracted gases dropped below 200°C inside the wall of the chamber. With the available suction flow rate of the pump (4 nL/min), the quenching rate is estimated to be around 10^5 K/s. However, this is two orders of magnitude lower than the rate found by Lallemant et al. [8] in order to have a correct measurement of intermediate species like CO. This gives rise to measurement errors, particularly in the reaction zone where the kinetic times are relatively fast. In order to evaluate the error margin caused by the quenching rate, we carried out several measurements in the reaction zone with and without cooling. When the probe was cooled, the sampling duration was about 2 min.

Table 1 presents the variation of the measurements of different species with and without introducing water to the probe. It is important to note that this variation is not uniquely caused by the quenching rate, rather, there are several factors inducing this variation. O_2 and CO_2 are measured with acceptable variation. However as expected, CO is highly influenced by the sampling process in the reaction zone. NO is less reactive than CO and the variation here could be mostly dependent on the gas analyzer accuracy. As a result, the measured composition can be fairly considered as representative of the gas composition at the sampling point.

Species	O_2	CO_2	CO	NO
With cooling	14.2%	6.4%	10875 ppm	138 ppm
Without cooling	14.5%	6.8%	9339 ppm	125 ppm
Measurement variation (% of the reading)	< 2%	< 5%	< 14%	< 10%

Table 1: Measurement variation of different species with and without cooling the probe

The probe is connected to a combustion gas conditioner where the gas is filtered and dried of combustion water and other condensable (tars). A fraction (2 nL/min) of the sampled gas is thereafter sent to an ECOM gas analyzer to measure the composition of O_2, CO, CO_2, NOx and SOx. Each measuring point (52 points in total) is the average of a 5-minutes sampling duration. The measurements start at each odd port from the axis of the chamber and offset 5 cm towards the wall. More points were collected in the region of interest where most of the devolatilization and volatile reactions occurred. Hence, the sampling points lie on four vertical axes parallel to the axis of the chamber, with an offset of 5 cm each. They will be referred to as axis_0, axis_5, axis_10, and axis_15 respectively.

3 FUEL PROPERTIES

The fuel choice is for the purpose of investigating the volatile matter content influence on the combustion process. Volatile matter is the major decomposition product of most biomasses and therefore, the combustion process depends mainly on its mass fraction. The latter can be varied using torrefaction at different temperature levels and specified residence times.

	Pine	***Pin-T***	***Pin-P***
Ash	*0.87*	*1.33*	*2.54*
VM	*81.22*	*73.62*	*44.83*
FC	*18.58*	*25.05*	*52.62*
C	*51.68*	*55.10*	*67.77*
H	*5.93*	*5.68*	*4.50*
N	*0.22*	*0.29*	*0.32*
O (by difference)	*41.27*	*37.52*	*25.15*
LHV (MJ/kg)	*18.45*	*19.74*	*25.30*

Table 2: Proximate and ultimate analysis of the tested fuels (% except LHV)

The fuel used in the experiments is pine, which was torrefied at 280 °C for 25 min and pyrolyzed at 450 °C for 15 min. The mass yield in the first production conditions (280 °C, 25 min) reached 78% (on dry basis), while the pyrolyzed pine production yield (at 450 °C, 15 min) was 32% (on dry basis). Table 2 lists the proximate and ultimate analysis of the fuels.

The size distribution is represented in figure 4 by a Rosin-Rammler distribution that fits the fuel

granulometry as measured using sieve analysis. The average diameter is 475 µm, 230 µm and 260 µm and the spread coefficient is 1.4, 0.89 and 0.84 for pine, Pin-T and Pin-P respectively.

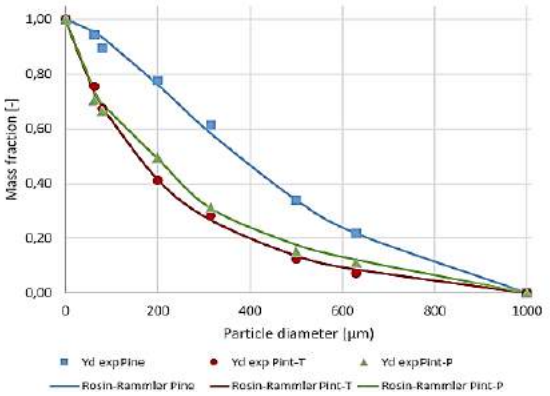

Figure 4: Particle diameter distribution of the tested fuels and their corresponding Rosin-Rammler fit

4 CFD MODELING OF PULVERIZED BIOMASS FLAMES

A CFD Fluent model is used to predict the flame characteristics and flow behavior of pulverized biomass injections in the pilot scale reactor. Due to the axisymmetric geometry of the reactor, the problem is reduced to a 2D axisymmetric geometry.

4.1 Particle combustion model

The particles injected in the computational domain are treated by a Lagrangian method called the discrete phase model (DPM) [9]. In the DPM, the particle's effect on the flow field is included in the continuous phase equations via source terms (two-way coupling). Therefore, the particles can exchange heat, mass and momentum with the gas stream. The strategy for the simulation is to alternate the Eulerian flow field and Lagrangian particle trajectory calculations until a converged coupled solution is obtained.

The DPM models present six laws that are alternately activated and deactivated along with the temperature and mass evolution of the particle: inert heating of the particle; water evaporation; water boiling; devolatilization; char surface oxidation; and particle cooling. With each law a series of equations are triggered to model the mass and heat transfer between the particle and the continuous phase. Devolatilization is modeled by a one-step Arrhenius mechanism. The model assumes that the process is a first step global reaction depending on the temperature of the particle (T_p) and the quantity of volatiles remaining in the particle:

$$\frac{dV}{dt} = A_v exp\left(-\frac{E_v}{RT_p}\right).(V_0 - V)$$

V_0 is the initial volatile content and V is the amount of the released volatiles. Av and Ev are the kinetic parameters. The surface oxidation law of the char (C) is modeled by a kinetic/diffusion limited model:

$$\frac{dC}{dt} = -A_c \frac{1}{\frac{1}{k_{diff}}+\frac{1}{k_c}} P_{O_2,g}^n$$

Where A_p is the particle surface area, $P_{O2,g}$ represents the oxygen pressure in the gas surrounding the particle, k_{diff} and k_c are the diffusion rate and kinetic rate respectively:

$$k_{diff} = D\frac{[(T_g+T_\infty)/2]^{0.75}}{d_p} \quad \text{and} \quad k_c = A_c exp\left(-\frac{E_c}{RT_p}\right)$$

D is the diffusion coefficient, while Ac and Ec are the kinetic parameters. The particle properties and the reactivity parameters are listed in table 3. The kinetic parameters of devolatilization and char oxidation were determined in a previous study in a drop tube furnace at high heating rate [10].

		Pine	Pin-T	Pin-P
Devolatilization parameters	Av [1/s]	248	250	2.81e+08
	Ev [J/kmol]	2.74e+07	3.2e+07	1.28e+08
Char oxidation parameter	C [-]	5.00e-13	5.00e-13	5.00e-13
	Ac [1/s]	9.2e-04	2.11e-03	113
	Ec [J/kmol]	6.35e+07	7.20+07	5.895+07
Volatiles molar mass		21.67	22.12	22.12
Swelling coefficient		0.754	0.795	0.774

Table 3: The reactivity parameters and particle properties for both fuels in the pilot-scale reactor

During devolatilization, the particle diameter (d_p) changes according to a user-defined swelling coefficient C_{sw}.

$$\frac{d_p}{d_{p,0}} = 1 + (C_{sw} - 1)\frac{(1 - f_{w,0})m_{p,0} - m_p}{f_{v,0}(1 - f_{w,0})m_{p,0}}$$

$f_{w,0}$ and $f_{v,0}$ are the initial moisture and volatile mass fractions respectively. The equivalent swelling coefficient was calculated from experimental data on the combustion of single particles of the tested fuels [11]. However, during the char oxidation, the kinetic/diffusion limited model uses a constant volume scenario. This scenario of volume evolution is proved to give similar results to those produced using an empirical model produced from experimental data [10].

4.2 Particle trajectory

The particle trajectory is described by the following forces: particle weight, Archimedes up-thrust and drag force. The latter is modeled here for a non-spherical drag law proposed by Haider and Levenspiel [12], which is found to perform among the best correction methods when applied to a multitude of shapes [13]. It can be implemented into the model to correct for the irregularity of the particle shape. This is necessary to describe the dispersion of the particles in the flow [14]. The velocity fluctuations are modeled using a Gaussian probability distribution and the variables obtained from the turbulence model.

4.3 Gas phase reactions

The gas phase is treated as a mixture of gases constituting air, biomass volatiles and combustion products. The gas phase reactions of volatiles are reduced into two-step mechanism that involves oxidation of volatiles to CO, CO_2 and H_2O in the first reaction (Rxn. (1)) and oxidation of CO to CO_2 in the second reaction (Rxn. (3)):

$$volatile + \vartheta_{O2}O_2 \rightarrow \vartheta_{CO}CO + \vartheta_{CO2}CO_2 + \vartheta_{H2O}H_2O + \vartheta_{N2}N_2 \quad (1)$$

$$char\ (s) + S_bO_2 \rightarrow CO \quad (2)$$

$$CO + \frac{1}{2}O_2 \rightarrow CO_2 \quad (3)$$

The CO oxidation reaction accounts for the CO produced by the char surface oxidation reaction. The volatiles are represented by the chemical formula $C_xH_yO_zN_w$, based on the molar fraction of carbon, hydrogen, oxygen and nitrogen in the volatile composition. These fractions are determined from the ultimate and proximate analysis of the biomass. The transport properties and the specific heats of the gaseous species were calculated using temperature dependent polynomial fits and the kinetic theory. Since the reactor operates at a constant atmospheric pressure, the density of the gas mixture was obtained from the incompressible-ideal-gas equation. The specific heat capacity was calculated using the mixing-law approach.

The turbulence is modeled using the realizable k-ε model, as it is the most appropriate model when turbulence transfer between phases plays an important role in gasification in the combustion chamber [15]. The Navier-Stokes equations are solved by introducing two new variables, the turbulent kinetic energy k and the turbulent kinetic energy dissipation rate ε. The reaction rate is calculated directly using the turbulence variables (k and ε) and the species concentrations. The turbulence-chemistry interaction is included in the simulations by the Finite-Rate/Eddy-Dissipation model, which performs well with simple reaction mechanisms. The model calculates both the Eddy-Dissipation reaction rate, and the reaction rate from the Arrhenius equation that is written for the mean flow variables, and takes the net reaction rate as the minimum of these two.

4.4 Radiation model

The heat transfer due to radiation is modeled using the discrete ordinate model (DOM). DOM allows activating the particle radiation interaction in the DPM to include the effect of radiation heat transfer to the particles. Simulations without including this interaction delayed the temperature rise of the particle but arrived at very high temperature values during char combustion, which caused a rapid conversion with the given kinetic parameters. Therefore, it is necessary to activate the particle radiation interaction for the DOM model to better predict the temperature rise of the particle and its reactivity.

4.5 Geometry and mesh construction

Due to the axisymmetric geometry of the reactor, the problem is reduced to a 2D axisymmetric geometry (Figure 5). The burner geometry is simplified to two 20 cm coaxial tubes corresponding to the real burner exit area.

A uniform organized mesh is created, which is more refined at the axis and gradually coarsened towards the wall. The biomass jet and the near bluff-body zone are especially refined to establish a well-detailed calculation about the internal recirculation zone and the near-burner zone phenomena. The mesh consists of 288191 nodes and 286400 quadrilateral cells. It retains high quality with minimum orthogonality of 0.99994 and maximum skewness of 6.7e-03.

4.6 Boundary conditions

The biomass jet is introduced to the domain through a surface injection normal to the burner central inlet. The size distribution is represented in *Figure 3* by a Rosin-Rammler distribution that fits the fuel granulometry as measured using sieve analysis. The particles are approximated as spheres of which their diameters are that of the sieving size. The complete range of particle sizes between 10 μm and 1000 μm is divided into 20 sets of discrete size ranges, each possessing a mass fraction calculated by the Rosin-Rammler distribution. A total number of 1400 particles were tracked in each case.

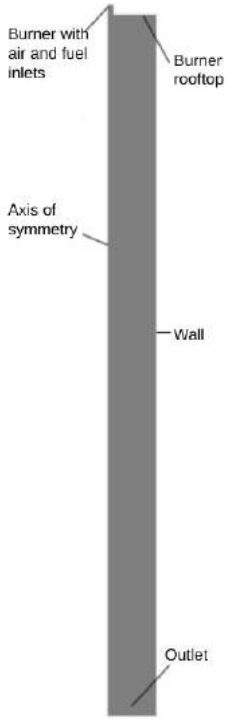

Figure 5: The simplified geometry of the 2D axisymmetric computational domain of the pilot-scale reactor

Case	**#1**	**#2**	**#3**
Fuel	Pine	Pin-T	Pin-P
Fuel feed rate	4.1 kg/h (~20.4kW)	3.7kg/h (~20.5kW)	3.1kg/h (~20.5kW)
Transport air velocity	14.74 m/s	14.74 m/s	14.74 m/s
Combustion air velocity	15.08 m/s	15.08 m/s	15.08 m/s
Combustion air temperature	380°C	380°C	380°C
Excess air	1.3	1.3	1.3

Table 4: Boundary conditions of the simulated cases

All walls were set to the steady-state temperatures measured experimentally by the thermocouples implemented in the walls. The chamber wall temperature is assigned via a user-defined function with the profiles shown in figure 2. The roof temperature is set to 400 °C and the bluff body temperature is assumed at the same temperature too. The burner walls temperature is approximated by the temperature of the secondary air

passing by.

Three cases were studied each for pine, torrefied pine and pyrolyzed pine respectively. The cases were made at iso-power, isokinetic and same excess-air conditions (Table 4). Although the different fuel load changes the particle-to-particle interaction, we consider under these conditions that the differences result only from the fuel properties.

4.7 Calculation methods

The calculations were conducted with the Pressure-Based Steady solver of ANSYS Fluent. It uses the finite volume method to solve the governing equations. The pressure and velocity were coupled with the coupled algorithm, and the pressure was discretized with the second order scheme. The energy, species, momentum, and turbulence equations were all discretized with the Second Order Upwind scheme. DOM equations were discretized with the First Order Upwind scheme. The pseudo transient algorithm is enabled, which adds an unsteady term to the solution equation in order to improve the stability and convergence behavior.

During the calculations, a continuous oscillation of the residuals was observed each DPM iteration. This can be resolved either by increasing the number of continuous phase iterations per DPM iteration or/and by reducing the under-relaxation factor of DPM. Both methods increase the stability but require more iterations to converge. The number of continuous phase iterations per DPM iteration was set to 5 and the under-relaxation factors of DPM, volatiles, and CO were adjusted to reduce the magnitude of the oscillations.

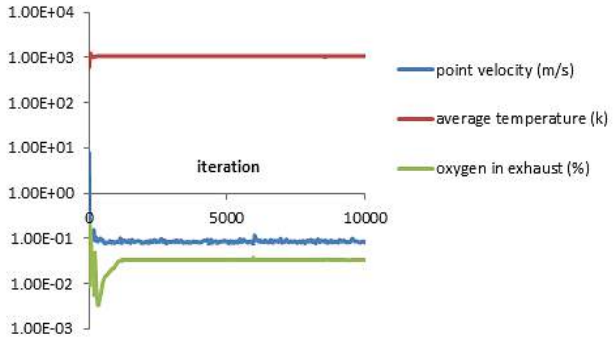

Figure 6: The monitored values of velocity, temperature and oxygen fraction during 10000 iterations (logarithmic scale on y-axis)

The convergence of the solutions was judged by monitoring the average temperature of the computational domain, the velocity at a defined point near the axis, and the mole fraction of oxygen at the reactor outlet. The calculations were stopped after the monitored values did not change between the iterations and the residuals had fallen below sufficient limits. Figure 6 shows the stability of the monitored entities during 10000 iterations of the pine combustion case.

5 RESULTS AND DISCUSSION

5.1 Model validation

The model predicts the flow dynamics, particle tracks and degradation history, the distribution of gas species concentration and reaction kinetics of the species. On the other hand, the experimental results provide the species concentration from probe sampling, and the flame topology from the chemiluminescence measurements. Analyzing the experimental data necessitates first to understand the aerodynamics generated by the burner and the trajectory of the particles. The degradation history of the particle is also important to explain the distribution of the species in the reactor and the reaction zones and their intensities. The aerodynamic features and particle history are predicted by the model, which needs to be validated first against the experimental data, before using them to characterize the simulated flames. Therefore, in this section, the measured gas species concentrations collected on the centerline of the reactor are compared to the predicted concentrations.

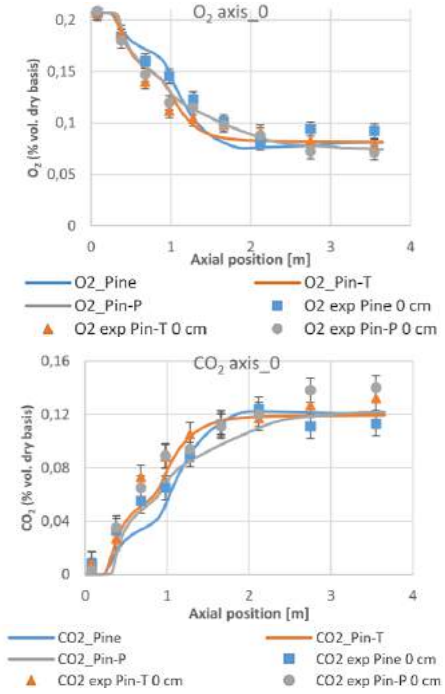

Figure 7: Comparison of the concentrations of O_2 (top) and CO_2 (bottom) measured experimentally (symbols) and the profiles predicted by the CFD model (lines)

Figure 7 compares the concentrations of O_2 and CO_2 measured experimentally on the centerline and the profiles predicted by the CFD model. The model reproduces fairly well the experimental data of oxygen consumption on the centerline, which reflects the fine procedure followed to determine the kinetic parameters.

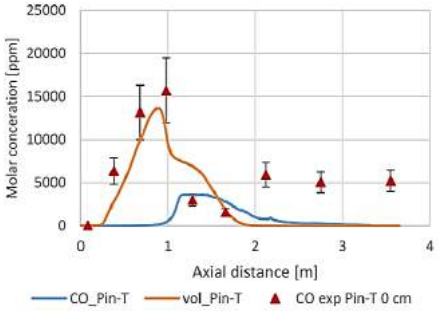

Figure 8: Prediction of the volatiles (vol) and CO molar concentration on the axis of Pin-T flame versus the measured CO molar concentration

CO_2 is slightly underestimated by the model but the deviation is still accepted considering the measurement

errors discussed previously, the used probe method without cooling overestimating the CO_2 concentrations (table 1). In addition, a slow surface oxidation model may also be another possibility, which increases the deviation between the experimental and numerical results. The reaction model adopted in the homogeneous phase of the CFD simulation is simplified, consisting of a two-reaction mechanism. The model considers CO as a product of oxidation of the volatiles rather than the major constituent of them. This shifts the predicted CO peak location from the real one as seen in figure 8. In fact, the real CO peak coincides with the simulated volatiles peak. The devolatilization model also well reproduces the beginning and the end of the volatile region. This means that the devolatilization kinetics are fine-tuned but the chemical kinetics of the homogenous phase reactions need optimization. Therefore, the predicted contours of CO and the experimental data do not represent the same parameter. As reactive species, uncertainty in CO concentrations by probe sampling has been also already mentioned (table 1). However, comparing the position of volatile release with the measured CO values verifies that the simplified devolatilization model can simulate the devolatilization correctly. Downstream the volatile flame, the predicted CO contours are not high enough where char combustion is taking place. This is probably due to fast reaction kinetics of CO in the simulation, which causes a rapid oxidation right after being produced by the surface reaction.

5.2 Flow dynamics and particles tracks

The contours of the axial velocity of the continuous phase obtained by flame simulation and presented in Figure 9 show aerodynamic features composed of a long jet, produced by the high injection velocities of the primary and secondary air.

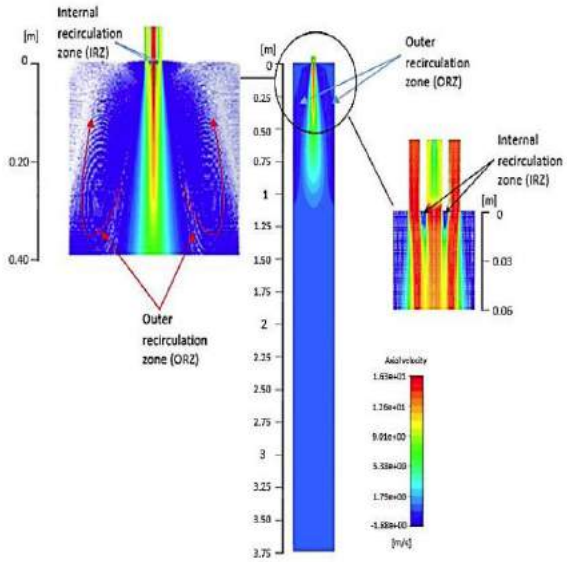

Figure 9: Axial velocity contours of the homogeneous phase for Pine flame

The jet decays progressively and a strong reverse flow appears behind, back to the roof where the recirculating flow is entrained again by the jet momentum. This creates as expected a large outer recirculation zone (ORZ) in the combustion chamber and a stagnant zone near the roof corners. This also helps bring the hot gas in the reaction zone back to the burner exit and promotes earlier devolatilization of the injected particles. The ORZ extends over 110 cm with its vortex core situated at 38 cm from the burner exit and at 13 cm off the chamber axis. Downstream the jet and the recirculation zones, the streamlines uniformly point toward the reactor exit with little turbulence. A close look to the burner region shows a low magnitude internal recirculation zone (IRZ) behind the bluff body, as intended by design. This allows the central jet to dominate and penetrate the IRZ. The central and annular jets open up right after injection and form shear layers with the IRZ, up to the meeting point about 5 cm ahead from the burner.

Figure 10 illustrates the particles trajectories in the reactive flow with different color shadings indicating the particle velocity. The particles are injected at zero velocity at the inlet and they are subsequently entrained by the transport air. Small particles acquire similar injection velocity as the carrier air, while large particles slip faster and enter the reactor at higher velocities. The stream of particles quickly scatters radially with the central jet with no interaction between the particles and the IRZ. They stay confined by the shear layer between the primary and secondary air streams, up to about 14 cm from the injection point. A simulation case was done using the same setup without activating the stochastic tracking of the particles. Most of the particles penetrated the recirculation zones and the reaction zone was pushed towards the reactor exit. However, when activated, the turbulence shows a significant impact on the particles trajectories. The aerodynamic flow and the particle trajectories are very similar, which means that the particles stick much more effectively to the fluid flow. Large particles are pushed by inertia down the reactor while smaller particles diverge with the air streamlines towards the outer recirculation zone and the furnace wall. Large eddies are formed by the recirculated particles back to the freshly injected secondary air. Only light ashes and the light chars at this point are entrained back to the top roof. That is why a low DPM concentration is present in this region.

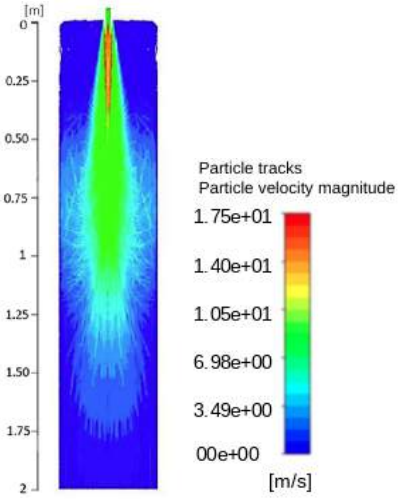

Figure 10: Trajectories of 1400 particles of Pine in reactive flow color-scaled by their velocities

5.3 Particle history: drying, devolatilization and surface oxidation

The described trajectories of the particles create the thermal and chemical conditions which the particles are

exposed to after injection. The degradation history and the morphological evolution of the particles play an important role in the competition between the body forces and the flow forces. These forces determine the particle velocity and trajectory. The figures below trace the trajectories of 1400 particles of pine, Pin-T and Pin-P. Three consequent time intervals are displayed; each corresponds to a different DPM law activated by each particle individually:

- Law 2: Particle drying tracks colored by the particle's moisture mass fraction (Figure 11)
- Law 4: Particle devolatilization tracks colored by the particle's volatile mass fraction (Figure 12)
- Law 5: Char surface oxidation tracks colored by the particle's fixed carbon mass fractions. (Figure 13)

Particle drying starts about 2 cm ahead of the injection point. However, the momentum and the thermal inertia of large particles elongate the drying zone. This zone is shorter for Pin-T considering its rapid heating due to small size and its low moisture content. The fact that small particles heats rapidly with lower inertia than large particles makes the drying length of Pin-P similar to pine, with twice the initial moisture content of the former but finer PSD (Figure 4).

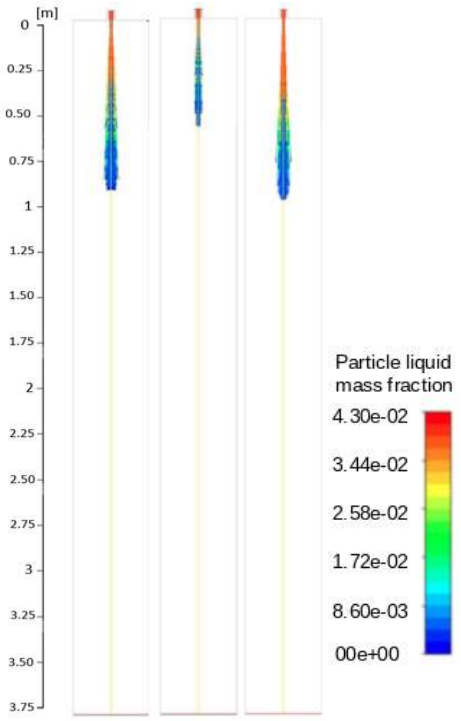

Figure 11: Particles trajectories during the drying stage colored by liquid mass fraction (single color scale, left to right: Pine, Pin-T and Pin-P flames)

As shown in figure 12, devolatilization already starts for small particles in the drying zone; nevertheless, most of the particles in the jet hold their volatiles in the drying zone. Once the activation energy is attained, the particles start the devolatilization. Particles that interact early with the secondary air stream heat faster and undergo their devolatilization outside the jet core. This is the case of some Pin-P particles showing some devolatilization in the shear layer. Also, pine and Pin-T particles have this effect further. The jet velocity decays eventually and the gases are recirculated back to the roof. At this stage, light devolatilizing Pin-T particles follow the airstreams to complete the devolatilization in the ORZ or proceed to char oxidation there. Pine particles are also diverted by air but with high momentum, they are less likely to reverse their axial direction and rather flow towards the wall. A large fraction of large pine particles is not affected and they continue to form a second volatile-rich zone. Such two-stage devolatilization has been reported by Ballester et al. [7] in biomass flames. It is also observed in co-combustion mode with high contribution of biomass [16]. Pin-P case is different as no streams are traced for devolatilizing particles in the ORZ. While some particles are diverted early towards the ORZ, they seem to be volatile free before advancing in the zone. Other particles are predicted to push further in the reactor, which can be explained by the lower calculated drag on the particles due to a higher predefined shape factor compared to the other cases. Large particles, which already dry over a long distance, end up with high velocity deposing their volatiles over a long distance as well. This can be also attributed to the effects at particle scale, where the severe thermal treatment induces more pores in the particle structure causing a smooth ejection of volatiles whenever the treated particle is exposed to heat [11].

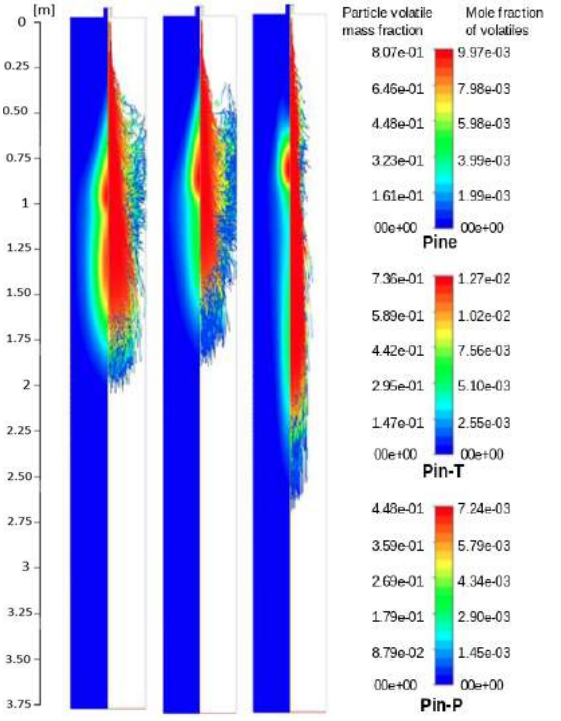

Figure 12: Particles trajectories during the devolatilization (right) colored by volatile mass fraction mirrored by the volatile mole fraction contours (left) (left to right: Pine, Pin-T and Pin-P flames)

Surface oxidation is activated at the end of devolatilization with certain overlap and it continues until the burnout. It is a long process and that is why the surface reaction law is found to be active almost everywhere in the reactor (Figure 13). Mainly, small char particles oxidize in the jet core or in the ORZ, while particles that dominate the aerodynamic effects burn in the lower part of the reactor. The heterogeneous reaction seems to be active near the walls. However, concentrating the particles near the wall might be caused by poor wall collision treatment in the simulations.

The global burnout of pine, Pin-T and Pin-P is estimated from the average CO_2 and CO concentrations measured in the effluent gases as 90%, 92.5% and 87% respectively. It should be noted that the char mass fraction is not a good indicator of the burnout of the particle. During char oxidation, the particle is mainly composed of char (fixed carbon) and small ash content. The char mass fraction is calculated as the ratio of the remaining carbon and the sum of ash and initial fixed carbon ($Char\ mass\ fraction = FC/(FC + ash)$). Fixed carbon is always dominant in front of the low ash content.

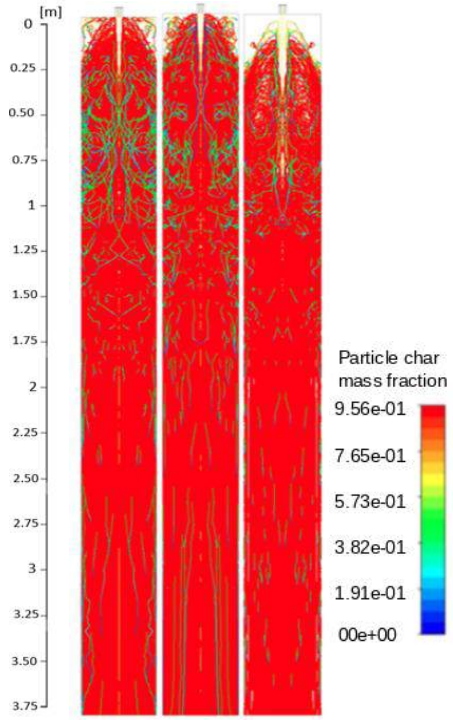

Figure 13*:* Particle trajectories during char oxidation colored by the char mass fraction (single color scale, left to right: Pine, Pin-T and Pin-P flames)

5.4 Flame development

Figure 14 shows the contours of the reaction rate of oxidation of volatiles in the three cases. All cases show a lifted long flame. This structure is due to the high injection velocity that shifts the devolatilization zone away from the burner and permits the jet to scatter and diffuse. The volatile zone emerges before the end of the drying phase. A volatile rich region is formed that subsequently diffuses and mixes with air in a thin layer triggering the oxidation. This layer of high reaction rate represents the flame front of the volatiles. A cross section of the OH* chemiluminescence images present in Figure 15 would give a similar profile to the flame front in Figure 14. Indeed, OH* chemiluminescence is an indicator of the heat release in gas flames, which means it is directly related to the zone of volatile oxidation reaction. The predicted reaction zones match well with the emission signal of the OH* chemiluminescence.

Both experiments and simulations indicate that the reaction starts at port 3 (z = 79 cm) where the particles start devolatilization. Large PSD increases the lift-off of pine while the flame front of Pin-P locates higher in the reactor than Pin-T despite having similar PSD and higher moisture content. The earlier reaction can be attributed to the low ignition temperature of Pin-P (220°C) compared to Pin-T (290°C) [11]. The reaction intensity grows progressively until reaching its peak at port 8 (z = 109 cm) in the case of Pin-T and Pin-P, while in Pine flames, OH* signal peaks at port 10 (z = 139 cm). This is attributed to the reaction zone of the volatiles of large particles of Pine. The reaction rate starts to decrease afterwards because the concentration of the remaining volatiles decreases, in addition to the depletion of available oxygen.

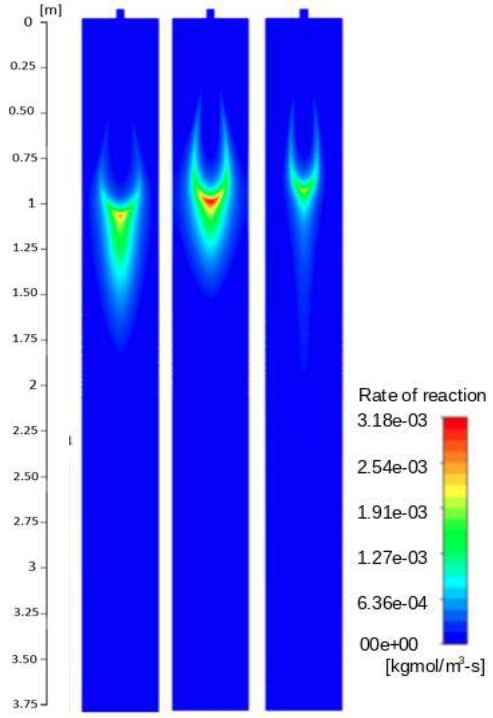

Figure 14: Reaction rate of oxidation of volatiles (single color scale, left to right: Pine, Pin-T and Pin-P flames)

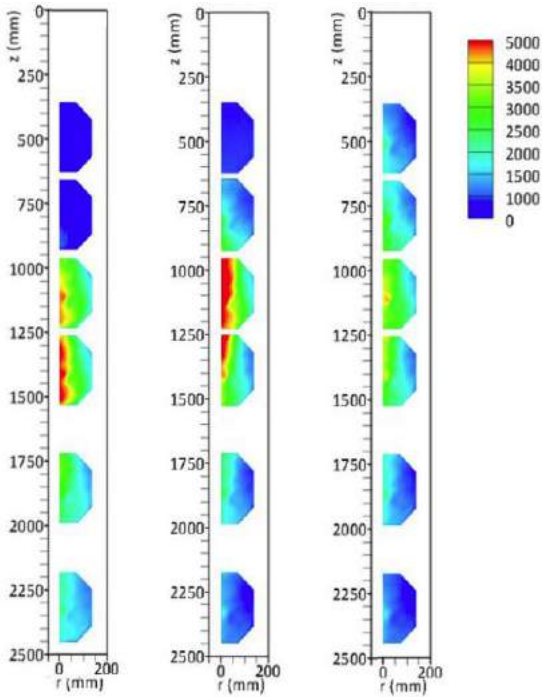

Figure 15: Average images of OH* chemiluminescence, (single color scale, left to right: Pine, Pin-T and Pin-P flames)

Pin-P flame contains less volatiles and the reaction is more diluted because of the long devolatilization trajectory. As a result, the OH* chemiluminescence intensity of Pin-P is relatively low. To the contrary, Pin-T emits more volatiles in a shorter distance and creates a rich volatile region as demonstrated earlier, which promotes the reaction rate in the flame front. A higher volatile content improves the diffusion of the combustible gases, causing intense oxidation and a larger flame volume.

Pine similarly has a large flame volume; however, the two-region devolatilization reduces the peak of reaction intensity despite having the highest volatile content. Small and large particles react in separate regions, diluting the chemical reaction.

5.5 Temperature field

Figure 16 presents the temperature contours in the pilot scale reactor for the three simulated flames. The injected air temperature heats first by the radiating walls and the hot recirculating gas. A point of deflection is detected after port 3 (z = 34 cm), which coincides with the onset of OH* chemiluminescence signal and oxygen consumption. This suggests that this temperature rise is caused by the heat liberated by the oxidation of volatiles. Pin-P shows earlier rise than Pin-T and Pine respectively in accordance with the chemiluminescence results. A peak is then attained firstly by Pin-P at 938°C, followed by the peak of Pin-T flame at 1013°C and Pine peak comes last with the highest value at 1056°C. A part of the gases is recirculated back to the burner entraining some particles, while the jet core develops towards the outlet. As a result, the temperature drops on axis_0 because a part of the heat is captured by the recirculation zone.

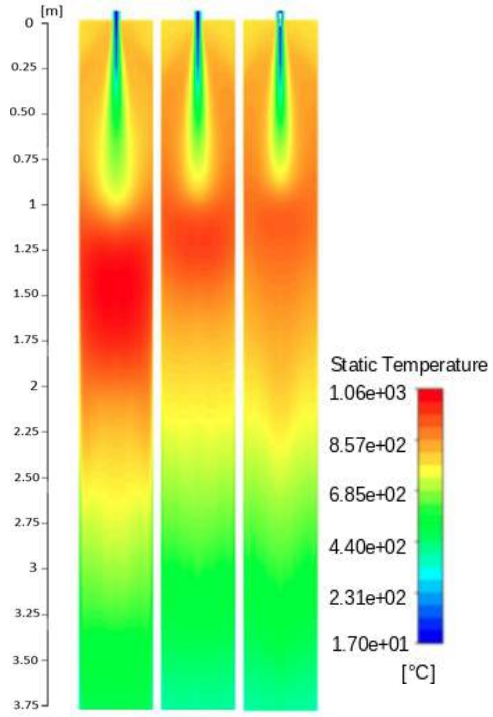

Figure 16*:* Temperature contours of the flames in the pilot scale reactor (single color scale, left to right: Pine, Pin-T and Pin-P flames)

As mentioned earlier, fewer Pine particles are recirculated with the streamlines to the ORZ, whence the higher temperature on the axis of Pine flames after the peak and consequently lower temperature is observed in the ORZ. On the other hand, Pin-T and Pin-P particles are more directed to the ORZ. Therefore, most of their energy is liberated there causing a higher temperature and a more efficient heating of the injected stream. After 2 m from the burner exit (port 13), the jet opens more behind the ORZ and the particles scatter radially. The heat release becomes more radially homogeneous causing less temperature gradient from the axis to the wall and flat radial temperature profiles.

5.6 Oxygen distribution

Figure 17 shows the contours of mole fraction of oxygen in the reactor. Figure 18 presents the comparison of the predicted oxygen profiles and the measured values along the four vertical axes. The model reproduces fairly well the experimental data, which reflects the fine procedure followed to determine the kinetic parameters. Right after injection, oxygen gets diluted by the liberated moisture and volatiles in the injected jet and by the recirculated gases in the ORZ. The consumption of oxygen takes place mainly in the flame front during the oxidation of volatiles. A short flame lift-off for Pin-T is marked by a rapid decrease in the oxygen concentration. Pine reactions are further on the axis where oxygen is largely consumed by the high concentration of volatiles. The oxygen reduction locates higher on the chamber axis for Pin-P but the consumption eases down later on, because of the long diluted devolatilization region.

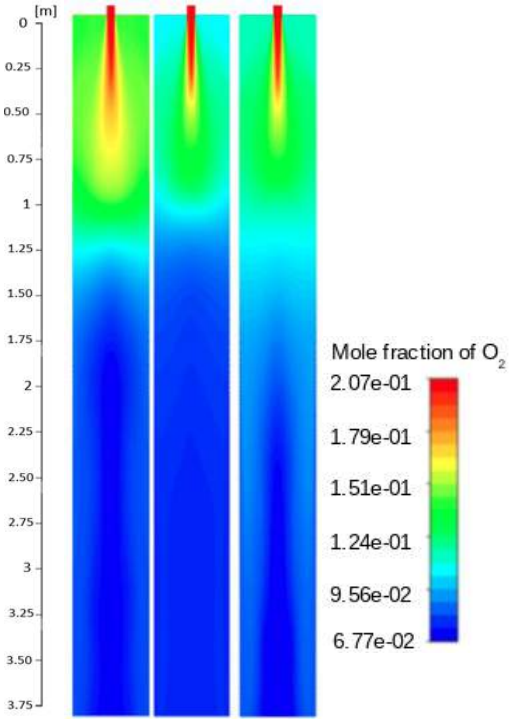

Figure 17: Oxygen contours of pine, Pin-T and Pin-P in the pilot scale reactor (single color scale, left to right: Pine, Pin-T and Pin-P flames)

However, one can notice from experiments and simulations that the oxygen molar fraction increases slightly as we approach the wall especially in the Pin-P case. The particle tracks of each fuel suggest that particles whose momentum is high enough to escape the aerodynamic effects are apt to stay in the center of the reactor afterwards. Consequently, the oxygen consumption is higher on the central axis and decreases

towards the wall. The gradient is bigger for Pin-P because Pin-P particles carry their volatiles to a long distance in the reactor as seen earlier, and even after complete devolatilization, they contain high fixed carbon content so they tend to be heavier than the chars of Pine and Pin-T.

Notice that the oxygen concentration on axis_2.5 exhibits a maximum approximately at the same position in the three cases, where it starts later to decrease. A similar profile is noticed experimentally and numerically on the other offset axes but the maximum is found further in the reactor as we approach the wall. The decrease in oxygen concentration happens in the ORZ and the maximum is at the point where the central jet reaches a 2.5cm radius and then further to 5 cm and so on. This means that the maximum is on the shear layer between the jet and the ORZ. This observation shows that the aerodynamics of the three flames is predicted satisfyingly well by the CFD model.

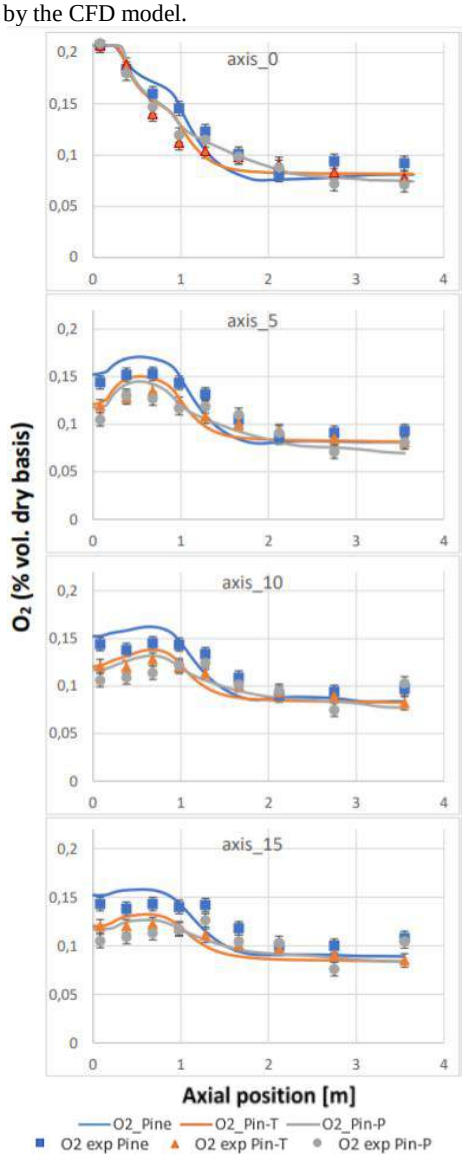

Figure 18: Comparison of experimental results and predictions of oxygen profiles on four vertical axes

Particles in the ORZ are mainly chars undergoing the heterogeneous surface reaction. Experiments measure low oxygen concentration for Pin-P in the ORZ, followed by Pin-T and finally pine with the highest oxygen concentration near the roof. The numerical results predict the same trend. This proves again that Pin-T and Pin-P are more influenced by the aerodynamics of the flame than pine. Char oxidation occurs over a long duration and it gets longer with the severity of the thermal treatment [11]. Particles captured by the ORZ are stuck in eddies there, so their residence time is sufficient to complete the burnout. However, large particles acquire high velocity and their reaction goes slowly over the last two meters of the reactor. This is the case of the majority of pine chars and the large particles of Pin-T and Pin-P. Therefore, oxygen consumption is slow in the lower section of the reactor, which explains the flatness of the profile at the end of every axis.

5.7 Carbon oxides distributions (CO and CO_2)

Figure 19 shows the measurements of CO on four vertical axes. In the three flames, CO peaks in the devolatilization region then decreases by oxidation, only to increase later as a product of the oxidation of char. The profiles strongly replicate the profiles observed in a previous study in the drop tube furnace [10].

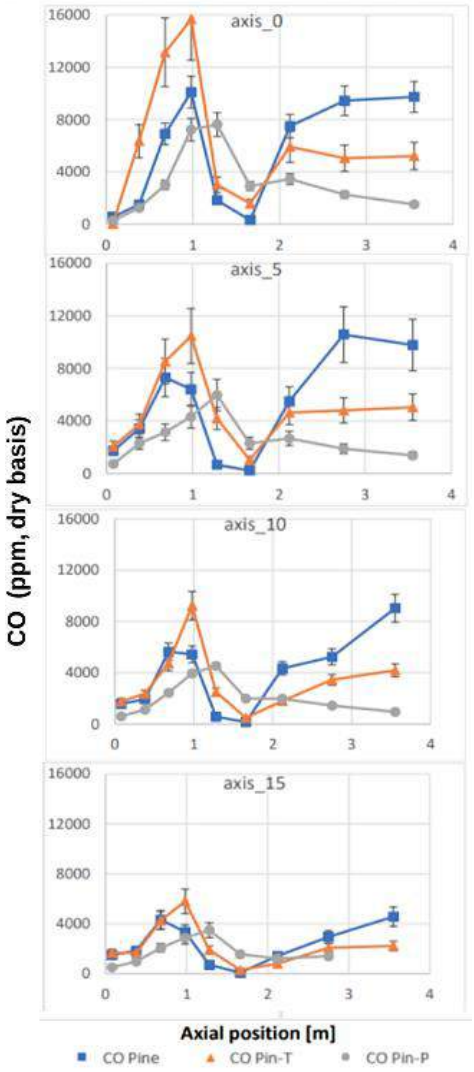

Figure 19: Experimental results of CO distribution on four vertical axes

A minimum is spotted at port 11 (z = 162 cm), where the flame front depletes and many particles either are in the ORZ or escape it to undergo char oxidation later. The

value of the minimum is dependent also on the overlap of the homogeneous and heterogeneous oxidations. A longer overlap would increase the CO production in the devolatilization zone preventing the CO level from going near zero as measured for Pine. Previous experimental investigations on the particles of the tested fuels in [11] have shown that the overlap increases with lower volatile content. The order of the CO minimum value at port 11 (z = 162 cm) validates this conclusion. Pine has a lower minimum, followed by Pin-T then Pin-P, indicating a minimum overlap for Pine and a maximum overlap for Pin-P.

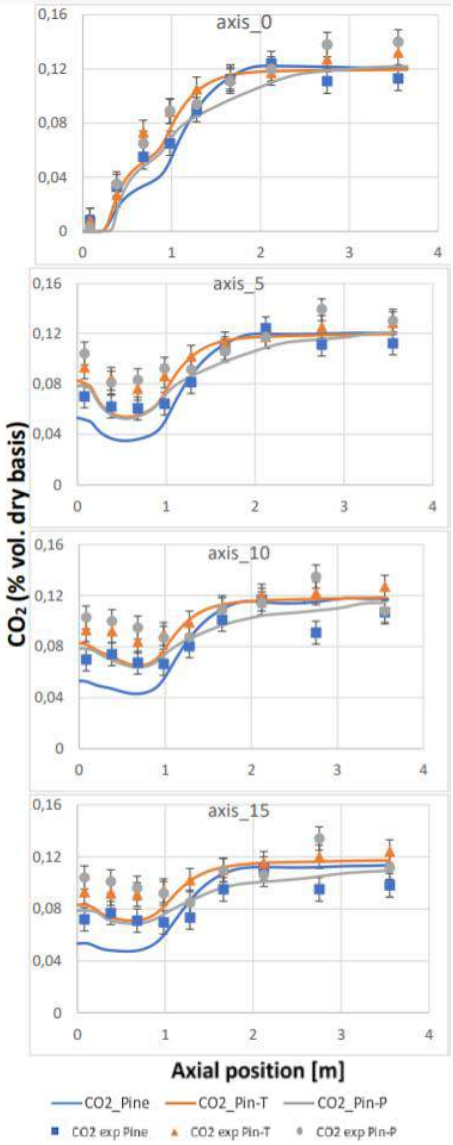

Figure 20: Comparison of experimental results and predictions of CO_2 profiles on four vertical axes

The CO peak position in the devolatilization zone is in accordance with the volatile contours presented earlier in Figure 14. Pin-P has the lowest maximum because of its low volatile content. Pine shows lower peak than Pin-T, which may be attributed to the distribution of Pine volatiles in two regions. Indeed, the second increase of CO after port 11 (z = 162 cm) is most probably due to char oxidation and the devolatilization of large particles. Instantaneous images of OH* chemiluminescence show signals coming from isolated particles of Pine at port 14 (centered at z = 231 cm), this suggests that these particles are enveloped by a flame.

Simulations seem to produce similar trends and carbon conversion rate as the experimental data of CO_2 but with some underestimation as can be seen in figure 20. CO_2 is directly related to the oxygen consumption considering that carbon forms more than 50% of the biomass. The trends are consistent with the data and the previous analysis of particle history. More CO_2 is produced by Pin-T and Pin-P in the ORZ than pine. CO traces are found there with no volatiles. This validates again that Pin-T and Pin-P particles follow better the airstream to undergo char oxidation in the ORZ. Moreover, exhaust gas compositions reveal lower carbon conversion for pine than Pin-T and Pin-P.

5.8 Nitrogen oxides distribution

The conversion mechanism of N to NO occurs through several routes during devolatilization and char oxidation.

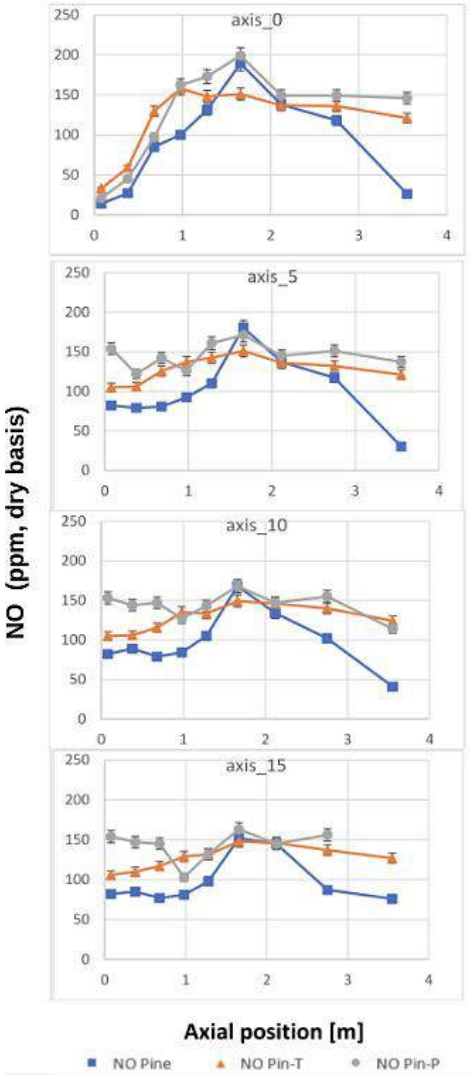

Figure 21: Experimental results of NO distribution on four vertical axes

Figure 21 plots the experimental results of the NO distribution on four vertical axes. The profiles on the central line increase during devolatilization. The three fuels reach their maximum approximately at the position of the temperature peak. This suggests that the thermal

route contributes to the total NOx concentration in the flame. Pine NO increases slower than the other fuels and peaks further in the reactor at the second devolatilization peak. Similarly, long devolatilization path explains the delayed peak of Pin-P. Unlike Pin-T and Pin-P, NO decreases significantly in pine flames after the peak. It seems that the devolatilization of large particles at the end of the reactor as confirmed by OH* chemiluminescence has a reducing effect on the NO concentration. NO precursors, mainly NHi and HCN, and other gases (CO and CHi) released during the devolatilization of large pine particles may be behind the reduction mechanism of NO in pine flames [17]. The staging of devolatilization may be a way of reducing NO levels in biomass-fired furnaces [7]. Pin-T and Pin-P also experience a relatively slight decrease in NO at the end, which is probably caused by the fast heterogeneous reaction of NO with the chars.

6 CONCLUSIONS

An experimental and numerical study of the combustion of pulverized biomass flames is performed in a pilot scale reactor. The reactor is a 20 kW downfired vertical chamber designed for the study of pulverized biomass flames. This experimental rig will make it possible to study biomass flames in response to industrial needs using large quantities of biomass like CSR, and agricultural residues. The experimental data includes a detailed description of the spatial distributions of the main species concentrations beside the OH* chemiluminescence images of the three flames of pine, Pin-T and Pin-P. These results are in accordance with the predictions of the CFD numerical model.

The studied flames are long lifted jet flames, forming a large outer recirculation zone behind the central jet in the combustion chamber. This structure is due to the high injection velocity that shifts the devolatilization zone away from the burner and permits the jet to scatter and diffuse. Fuels with finer particle size distribution (Pin-T and Pin-P) are found to be more influenced by the aerodynamic structures, since their particles follow better the flow streamlines. Their devolatilization occurs in the jet and the chars are captured by the ORZ where they get oxidized. This creates a high temperature in the ORZ, which helps heat up the injected particles. On the other hand, the wide particle size distribution of pine manifests in two-devolatilization stages, and the large particles tend to penetrate the recirculation zone and oxidize downstream.

The volatiles start to react with oxygen in the flame front, which appears in the mixing layer of the fuel and air jets. The predicted reaction zones of the three flames obtained by CFD coincide well with the OH* chemiluminescence images. The topology and intensity of the latter is determined by the volatile content of the fuel and its reactivity. The particle size distribution also plays a key role. Pin-T with fine PSD shows the highest reaction intensity despite a lower volatile content than Pine. The two-devolatilization regions of pine reduce the reaction intensity, while that of Pin-P is more diluted and consequently less intense.

The results show that CO peaks in the devolatilization region, and increases later as a product of char surface oxidation. CO curves have a minimum between the two combustion stages, whose value reflects the degree of overlap of the devolatilization and char oxidation phases of each fuel: Pin-P has higher overlap than Pin-T and Pine respectively. NOx concentration measurements suggest that it is produced through fuel and thermal routes with high temperature sensitivity. Higher levels are measured in the middle of the reactor where it exhibits higher local temperature associated with thermal NO production on top of fuel NO formation. NOx levels decrease after the flame region. The reduction is slight for Pin-T and Pin-P while it is significant for pine due to the second devolatilization stage.

7 REFERENCES

[1] T. Wiesenthal, A. Mourelatou, J.-E. Petersen, and P. Taylor, “How much bioenergy can Europe produce without harming the environment?,” European Environment Agency, Copenhagen, 7, 2006, Jun. 2006.

[2] “Veolia solutions: biomass energy mix.” [Online]. Available: https://www.veolia.com/en/solution/biomass-energy-mix. [Accessed: 04-May-2020].

[3] “Ontario Power Generation, Canada Coal to biomass journey furnace,” Atitokan & Thunder Bay, Ontario, Canada, 2018.

[4] U. Nowling, “Successful Torrefied Biomass Test Burn at a Coal Power Plant,” University of Missouri-Kansas City, 2018.

[5] A. Elfasakhany, L. Tao, B. Espenas, J. Larfeldt, and X. S. Bai, “Pulverised wood combustion in a vertical furnace: Experimental and computational analyses,” Appl. Energy, vol. 112, pp. 454–464, Dec. 2013.

[6] R. Weber, Y. Poyraz, A. M. Beckmann, and S. Brinker, “Combustion of biomass in jet flames,” Proc. Combust. Inst., vol. 35, no. 3, pp. 2749–2758, 2015.

[7] N. Lallement, J. Dugue, and R. Weber, “Measurement techniques for studying oxy-natural gas flames,” Journal of the Energy Institute, vol. 76, no. 507, pp. 38–53, Jun. 2003.

[8] Fluent Inc., Fluent theory guide: Discrete phase models. Ansys Inc., 2001.

[9] H. Mohanna, J.M. Commandré, B. Piriou, B. Taupin, G. Vaitilingom, and D. Honoré, “Derivation of the kinetics of devolatilisation and oxidation of pulverized biomass in a drop tube furnace: Sensitivity to volume evolution and drag-coefficient model,” Fuel, vol. 293, p. 120434, Jun. 2021.

[10] H. Mohanna, J.M. Commandre, B. Piriou, G. Vaitilingom, B. Taupin, and D. Honore, “Shadowgraphy investigation of the combustion of raw and pre-treated single biomass particles: Influence of particle size and volatile content,” Fuel, vol. 258, p. 116113, Dec. 2019.

[11] A. Haider and O. Levenspiel, “Drag coefficient and terminal velocity of spherical and nonspherical particles,” Powder Technol., vol. 58, no. 1, pp. 63–70, May 1989.

[12] M. Mandø, L. Rosendahl, C. Yin, and H. Sørensen, “Pulverized straw combustion in a low-NOx multifuel burner: Modeling the transition from coal to straw,” Fuel, vol. 89, no. 10, pp. 3051–3062, Oct. 2010.

[13] N. Niemelä, “Computational fluid dynamics

modeling of pulverized biomass combustion using optimized reactivity parameters," Master thesis, Tampere University of Technology, 2015.
[14] A. Elorf and B. Sarh, "Excess air ratio effects on flow and combustion characteristics of pulverized biomass (olive cake)," Case Studies in Thermal Engineering, vol. 13, p. 100367, Mar. 2019.
[15] J. Ballester, J. Barroso, L. Cerecedo, and R. Ichaso, "Comparative study of semi-industrial-scale flames of pulverized coals and biomass," Combust. Flame, vol. 141, no. 3, pp. 204–215, May 2005.
[16] B. Damstedt, J. M. Pederson, D. Hansen, T. Knighton, J. Jones, C. Christensen, L. Baxter, and D. Tree, "Biomass cofiring impacts on flame structure and emissions," Proc. Combust. Inst., vol. 31, no. 2, pp. 2813–2820, Jan. 2007.
[17] T. Nussbaumer, "Primary and Secondary Measures for the Reduction of Nitric Oxide Emissions from Biomass Combustion," in Developments in thermochemical biomass conversion, A. V. Bridgwater and D. G. B. Boocock, Eds. Dordrecht: Springer Netherlands, 1997, pp. 1447–1461.

8 ACKNOWLEDGEMENTS

The authors acknowledge the financial support of the Association Nationale de la Recherche et de la Technologie in France (ANRT) (Convention CIFRE - N° 2016/0523).